Azimuthal anisotropy in elastic and equivalent media

Sitamai W. Ajiduah, Gary F. Margrave and P. F. Daley

ABSTRACT

A seismic numerical modeling experiment has been conducted to acquire a wide azimuth 3D-3C seismic data from an isotropic heterogeneous elastic model and an anisotropic homogeneous equivalent model in order to verify the suitability of these two modeling approaches for anisotropic studies. This study focuses on reflection amplitude and traveltime comparison of the two models. Although, geophysicists often prefer to use anisotropic homogeneous equivalent models for various seismic modeling and imaging tasks, there are however some benefits of heterogeneous models over anisotropic homogeneous equivalent models. We show that the anisotropic equivalent modeling predicts strong interbed multiples and multimodes which are much weaker in the heterogeneous elastic model. This is because a heterogeneous medium will cause irregular scattering of multiples and multimode events, thus diminishing these events. Both modeling results reveals AVAZ signatures which shows more significant azimuthal variations in the elastic model than in the equivalent model because of the strong multimode conversions which tend to obscure primary reflections at far offsets. Also, we investigated the effect of offset on PP and PS azimuthal anisotropy from the two HTI models with the aim of using the modeling results as guidance in seismic data application. AVAZ analysis shows that the major axes of the radial-component PS-wave amplitude elliptical fit are perpendicular to the fracture strike, which is opposite to the PP-wave amplitude elliptical fit whose major axes are parallel to the fracture strike. The azimuthal interval traveltime shows poor elliptical distribution, making it is difficult to use the interval traveltime analysis for the diagnostic use of fracture orientation. There is an offset limitation for both PP- and PS-waves traveltime fracture-induced anisotropy in both modeling. We observe also that PS-wave amplitudes from both models show a wider applicable offset range and larger observable azimuthal anisotropy than PP-waves.

INTRODUCTION

Fractures are one of the most abundant visible structural features in the Earth's upper crust, and they strongly influence seismic wave propagation, which give rise to fracture-induced anisotropy. They can affect porosity and permeability of reservoirs. Therefore, fracture detection and the estimation of fracture properties are important for reservoir characterisation, hydrocarbon production and CO_2 storage. Studies have shown that azimuthal variation in seismic attributes (such as velocity, amplitude, and frequency) of P and S-wave data can be used as an indicator of azimuthal anisotropy (Daley and Hron, 1977; Ruger 1996; Bakulin et. al. 2000; Qian et al., 2007; Mahmoudian, et. al. 2013; Al Dulaijan et. al. 2016). Parallel vertical crack orientations can occur when the vertical stress becomes greater than the minimum horizontal stress. A medium containing vertically aligned fractures with scale length much less than the scale of the seismic wavelength can be modelled by an equivalent azimuthally anisotropic medium. The use of azimuthal seismic anisotropy to detect natural fractured reservoirs using equivalent medium theory

has been studied by many authors (e.g. Hudson, 1981; Schoenberg and Douma, 1988; Liu et. al 2000).

We used a staggered-grid finite-difference numerical modeling scheme to generate synthetic three-component 3D datasets and study the amplitude and traveltime responses for both the isotropic heterogeneous elastic model and anisotropic homogeneous equivalent media and compared the results from the two models. The HTI parameters of the anisotropic equivalent medium were obtained from a linear slip model proposed by Schoenberg and Muir (1989) and tested and verified by Carcione et. al. (2012) for any general anisotropic medium by numerical simulation. We also studied the effect of offset-depth ratio on the feasibility of performing azimuthal anisotropy analysis on PP and converted-wave PS data, with the aim of using the modelling results as guidance for future modeling, processing and interpretation of anisotropic response of orthorhombic models with finely layered overburden.

Schoenberg and Muir Theory

Backus (1962) presented an elegant method of producing the effective constants for a thinly layered medium composed of either isotropic or anisotropic elastic layers. This method applies either to spatially periodic layering or to random layering, by which we mean either that the material constants change in a non-periodic (unpredictable) manner from layer to layer or that the layer thicknesses might also be random. For applications to porous earth materials, we implicitly make the typical assumptions of spatial stationarity within these layers as well as scale separation -- i.e., the sizes of the pores are much smaller than the thickness of the individual layers in which they reside. The key idea presented by Backus is that these equations can be rearranged into a form where rapidly varying (in depth) coefficients multiply slowly varying stresses or strains. Backus averaging is often applied to well logs in order to estimate the elastic properties of a stack of thin layers at a longer wavelength to be used in seismic data analysis. Schoenberg and Muir (1989) extended the Backus average approach to develop a matrix formalism that enables a simple calculation of the stiffnesses of the rock, and then achieves a description for the composition and decomposition of the effective anisotropic medium. Under the Backus theory (1962), a numerical simulation was performed to show that the Schoenberg-Muir theory is valid from the kinematic (traveltimes) and dynamic (amplitudes) viewpoints for a small crack aspect ratio or fracture opening, very long flat parallel fractures and thin layered media (Carcione et al., 2012). It concludes that a fracture as an infinitely extended weakness plane is an element for assembling a fractured medium from a fracture and a host medium. A fractured medium can be separated into a fracture and a host medium. In this view, a vertically fractured HTI medium consists of a vertical linear slip interface (a vertical fracture) and an isotropic homogeneous host medium (see figure 1). Also a more realistic orthorhombic medium can be formed by either embedding a vertical slip interface into a transversely isotropic host medium with a symmetric vertical axis (VTI) or embedding a horizontal slip interface into a transversely isotropic host medium with a symmetric horizontal axis (HTI)

1. An azimuthal scan is a circle of seismic traces having a common source-receiver offset for all azimuths and obtained by 2D interpolation of traces at every azimuth for each time samples. 2. Radial scan is a line of seismic traces having a common azimuthal

angle for all source-receiver offsets and obtained by 2D interpolation of traces at every radial distance from the source for each time samples.

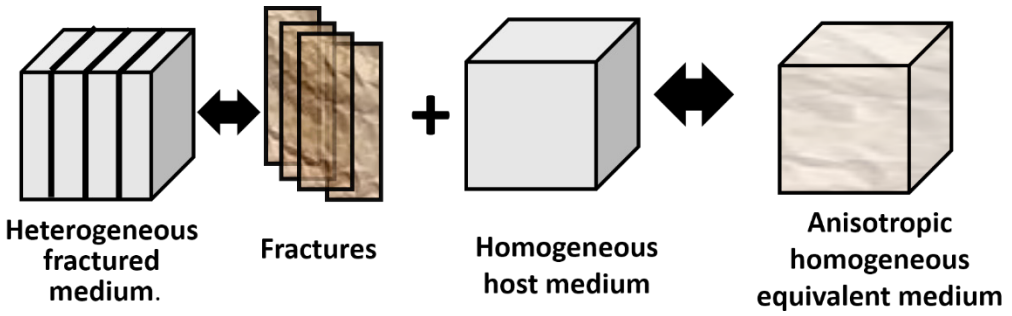

$$C = C_{iso} + \Delta C_{ani}$$

Fig 1: Linear slip model for vertical fractured media.

Let us consider a finely layered medium composed of N arbitrarily isotropic layers with the z-axis perpendicular to the layering plane. Each layer is defined by the density ρ, the layer thickness H_n, and the elastic constants C_{ij}. In the long wavelength limit, all components of stress acting on the layering plane, i.e. σ_{3h}, σ_{4h} and σ_{5h} (where $h = 1 \cdots n$ with h denoting different layers) and all components of strain lying in the layering plane, i.e. $e_{1h}, e_{2h}, and\ e_{6h}$ a, are the same in all the layers across medium H. The notations of stress and strain are in Voigt form. The other components of the stress and strain, i.e. $\sigma_{1h}, \sigma_{2h}\ and\ \sigma_{6h}$ and $e_{1h}, e_{2h}, and\ e_{6h}$ are different from layer to layer. In other words, some components of stress and strain are layer-independent. The stress-strain relation of each layer can be written as;

$$\begin{pmatrix} \sigma_1 \\ \sigma_2 \\ \sigma_6 \\ \\ \sigma_3 \\ \sigma_4 \\ \sigma_5 \end{pmatrix} = \begin{pmatrix} \sigma_{11} \\ \sigma_{22} \\ \sigma_{12} \\ \\ \sigma_{33} \\ \sigma_{23} \\ \sigma_{13} \end{pmatrix} = \begin{pmatrix} c_{11} & c_{12} & c_{16} & c_{13} & c_{14} & c_{15} \\ c_{12} & c_{22} & c_{26} & c_{23} & c_{24} & c_{25} \\ c_{16} & c_{26} & c_{66} & c_{36} & c_{46} & c_{56} \\ & & & & & \\ c_{13} & c_{23} & c_{36} & c_{33} & c_{34} & c_{35} \\ c_{14} & c_{24} & c_{46} & c_{34} & c_{44} & c_{45} \\ c_{15} & c_{25} & c_{56} & c_{35} & c_{45} & c_{55} \end{pmatrix} \begin{pmatrix} e_1 \\ e_2 \\ e_6 \\ \\ e_3 \\ e_4 \\ e_5 \end{pmatrix}, \qquad 1$$

where $\sigma_1, \sigma_2\ and\ \sigma_6$ and $e_3, e_4\ and\ e_5$ denotes the layer-dependent stress and strain components. Also σ_3, σ_4 and σ_5 and $e_1, e_2, and\ e_6$ are the layer-independent stress and strain components in Voigt notation. The stiffness matrix involved in equation 1 can be rewritten in terms of four submatrices as

$$\begin{pmatrix} C_{TT} & C_{TN} \\ C_{TN}^{\dagger} & C_{NN} \end{pmatrix}, \qquad (2)$$

The layer dependent term (represented with an accent) and layer independent term of the stress strain is obtained below.

$$\bar{\sigma} = C_{TT}e + C_{TN}\bar{e}, \quad (3)$$

$$\sigma = C_{NT}e + C_{NN}\bar{e}\,, \quad (4)$$

According to Schoenberg and Muir (1989), the equivalent homogeneous medium is defined by:

$$\begin{pmatrix} \bar{C}_{TT} & \bar{C}_{TN} \\ \bar{C}_{TN}^{\dagger} & \bar{C}_{NN} \end{pmatrix}, \quad (4)$$

$$\bar{C}_{NN} = \langle \bar{C}_{NN}^{-1} \rangle^{-1},$$

$$\bar{C}_{TN} = \langle C_{TN} {C_{NN}}^{-1} \rangle \bar{C}_{NN},$$

$$\bar{C}_{TT} = \langle C_{TT} \rangle - \langle C_{TN} {C_{NN}}^{-1} C_{NT} \rangle + \bar{C}_{TN} \langle \bar{C}_{NN}^{-1} C_{NT} \rangle, \quad (5)$$

where the thickness weighted average of a quantity C is defined in terms of relative layer thickness H and individual layer stiffnesses as

$$\langle C \rangle = \sum_{n=1}^{N} H_n C_n, \quad (6)$$

We considered periodic systems of equal composition whose single layers have transversely isotropic symmetry. The analytical equations for isotropic and transversely isotropic layers are given below for the case where individual layer is isotropic.

$$C_{33}^{e} = \langle \frac{1}{C_{33}} \rangle^{-1}\,, \quad (7a)$$

$$C_{44}^{e} = C_{55}^{e} = \langle \frac{1}{C_{44}} \rangle^{-1}\,, \quad (7b)$$

$$C_{13}^{e} = C_{23}^{e} = \langle \frac{C_{12}}{C_{33}} \rangle \langle \frac{1}{C_{33}} \rangle^{-1}\,, \quad (7c)$$

$$C_{66}^{e} = C_{66}\,, \quad (7d)$$

$$C_{11}^{e} = C_{22}^{e} = \langle C_{11} \rangle + \langle \frac{C_{12}}{C_{33}} \rangle^{2} \langle \frac{1}{C_{33}} \rangle^{-1} - \langle \frac{C_{12}^{2}}{C_{33}} \rangle\,, \quad (7e)$$

$$C_{12}^{e} = \langle C_{12} \rangle + \langle \frac{C_{12}}{C_{33}} \rangle^{2} \langle \frac{1}{C_{33}} \rangle^{-1} - \langle \frac{C_{12}^{2}}{C_{33}} \rangle = C_{11}^{e} - 2C_{66}^{e}\,. \quad (7f)$$

There are a total of five independent non-zero elements ((7a–7e) in the stiffness matrix of the equivalent medium and they are of the VTI type. This means if individual layers are isotropic, the long wavelength equivalent medium will be VTI. Note that there are only two independent parameters in an isotropic medium: $C_{11} = (\lambda + 2\mu)$ and $C_{66} = \mu$ where λ and μ are the Lame parameters. Also, $C_{12} = C_{11} - 2C_{66}$, $C_{33} = C_{11}$, $C_{44} = C_{55} = C_{66}$, and $C_{13} = C_{12} = C_{23}$. Equations (7a) to (7f) are equivalent to the Schoenberg and Muir (1989) averaging method of equation 5 above. The equivalent VTI system is then rotated clockwise through angle $\beta = \pi/2$ about the x_1 axis by an orthogonal transformation

matrix to obtain an HTI equivalent medium. The HTI stiffnesses are related to Thomsen-style anisotropy parameters along the x_2 symmetry axis: - by $V_{p0} = \sqrt{C_{33}/\rho}, V_{s0} = \sqrt{C_{55}/\rho}, \varepsilon^v = (C_{33} - C_{11})/2C_{11}$, $\gamma^v = (C_{44} - C_{55})/C_{55}$ *and* $\delta^v = ((C_{13} + C_{55})^2 - (C_{33} - C_{55})^2)/2C_{55}$. The fast and slow shear waves are expressed as $Vs_{slow} = V_{so} = \sqrt{C_{33}/\rho}$ and $Vs_{fast} = \sqrt{C_{44}/\rho} \approx V_{so}(1 + \gamma^v)$ respectively, where ε^v, γ^v *and* δ^v are the Thomsen's anisotropy parameters.

Seismic forward modeling of fractures

SINTEF TIGER staggered-grid finite-difference modeling was used to generate 3C-3D synthetic datasets. The datasets were then rotated into radial and transverse component for further analysis. Figure 2 shows the schematics of shear-wave splitting for isotropic and azimuthally anisotropic (HTI) case. In the presence of azimuthal anisotropy such as in figure 2b, the polarization is no longer determined by acquisition geometry but by the natural axes of the anisotropic medium (Bale et.al. 2009). In this figure the incident P-wave converts to an S_v wave at the top and bottom of the reflector and becomes polarized according to the anisotropy (stress or fracture) orientation thereby splitting into a fast (S1) shear wave with polarization parallel to the fractures and slow (S2) shear wave polarization, orthogonal to fracture strike. The difference in wave speed for these two modes causes them to become separated in time, each arriving with their distinctive polarization at the receiver location. Thus the waves carry the imprint of the anisotropic medium.

To better visualize, the 'signature' of shear-wave splitting as observed in 3D multicomponent surveys. Figure 2b is the model geometry in plan view. The fractures, oriented East at 0 degrees to symmetry plane, are shown as a hashed circle. At the centre is the conversion point of the effective shear wave source point. The black arrows are the orientation of radial and transverse receivers at constant offset from the source point. When the radial P-SV wave encounters this anisotropic medium, it splits (Figure 2b) into fast (red) and slow (blue) modes. The green axis (Figure 2c) parallel to the fractures, is the 'isotropy plane' and the orange axis is the 'symmetry-axis plane'. For shear waves aligned with either axis of the natural coordinate system there is no splitting. Hence, along the two symmetry planes we see the full amplitude of the original P-SV wave, with some time difference. At any intermediate azimuth, P-SV wave is split into two components (S1 and S2). The resulting amplitudes are illustrated by the coloured ellipses, with the S1 amplitude dropping to zero in the symmetry-axis plane and the S2 amplitude dropping to zero along the isotropy plane.

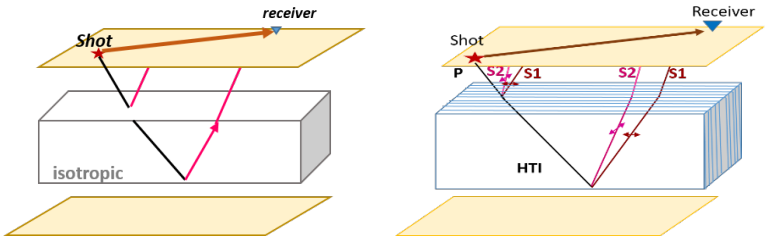

(i). Isotropic medium (ii). HTI medium

Figure 2a. A schematic diagram showing the absence and presence of shear wave birefringence in isotropic medium (i) and HTI medium (ii) respectively. (modified after Bale et. al, 2009).

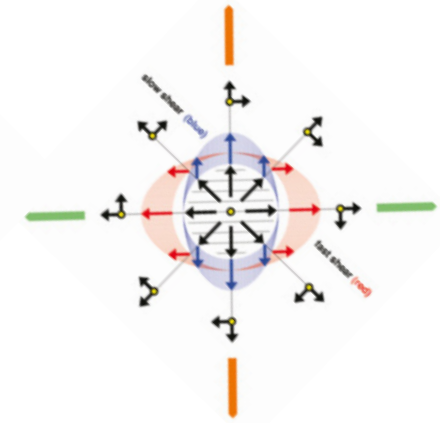

Figure 2b. Illustration of shear wave splitting on radial component. The fast and slow amplitude variation is shown in red and blue respectively, relative to the isotropy (green) and symmetry-axis (orange) planes (Bale et.al. 2009).

Method

Figure 3 shows the three-layer model used in this synthetic study. A periodic isotopic heterogeneous elastic fractured model (hereafter simply referred to as an elastic medium) and an anisotropic homogenous equivalent medium (hereafter simply referred to as an equivalent medium) were created. The top layer and bottom layer are isotropic, while the second layer is a 400m thick HTI layer modeling vertical fracturing. Fracture spacing is at a 20m interval and fracture strike is 0 degrees in the azimuthal plane. The offset range is from 20m to 2000m. The source, an explosive P-source with a 15 Hz Ricker spectrum, is located at the centre of the model, at depth 40m. This gives full azimuthal coverage through all 360 degrees. 3C receivers were placed on each of the grid points and buried at source depth. 3D shot records were generated for both the elastic and the equivalent model and azimuthal variation of PP and PS-converted reflections and interval traveltime were analysed for reflections from the top and bottom of the fractured middle layer. The interval traveltime means the time interval between the top and bottom of the fractured medium. The parameters of equivalent model and elastic model are shown in Table 1 below. Modeling was done with a grid size of 201x201x101. Figure 3b shows a brief workflow. The recorded 3D Z, X, Y datasets were later bandpass filtered and rotated into ZRT components. We then applied a 2D linear interpolation at every time-slice and translate the dataset from its acquisition domain to the offset-azimuth domain in order to obtained azimuthal scans[1] and radial scans[2] of datasets ($Z_{(t,r,\varphi)}$, $R_{(t,r,\varphi)}$ and $T_{(t,r,\varphi)}$) for further amplitude/time picking analysis and interpretations.

Table 1: Parameters of Model used in modeling.

	Heterogeneous elastic model	Anisotropic equivalent model

Layer1	$Vp = 3500m/s, Vs = 2140m/s, \quad \rho = 2200kg/m^3$	same
HTI Layer	$Vp_1 = 4700m/s, Vs_1 = 3980m/s, \rho_1 = 2500kg/m^3$ $Vp_2 = 4210m/s, \ Vs_2 = 2430m/s, \rho_2 = 2300kg/m^3$	$Vp_0 = 4438m/s, Vs_0 = 2762m/s, \rho^e = 2401kg/m^3$ $\epsilon^e = .0034, \gamma^e = .0607, \delta^e = -.0545$
Layer3	$Vp = 5000m/s, Vs = 3300m/s, \rho = 2900kg/m^3$	same

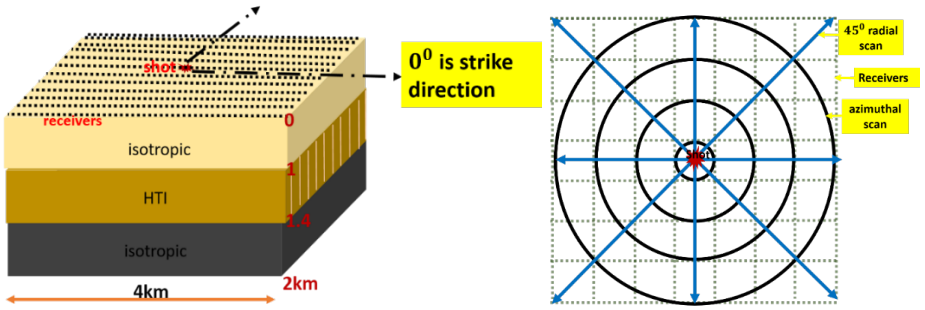

Figure 3a. Three-layer model and survey geometry (left) of shot and receivers showing fracture strike directions. The diagram on the right shows the plan view of what the azimuthal and radial scans look like.

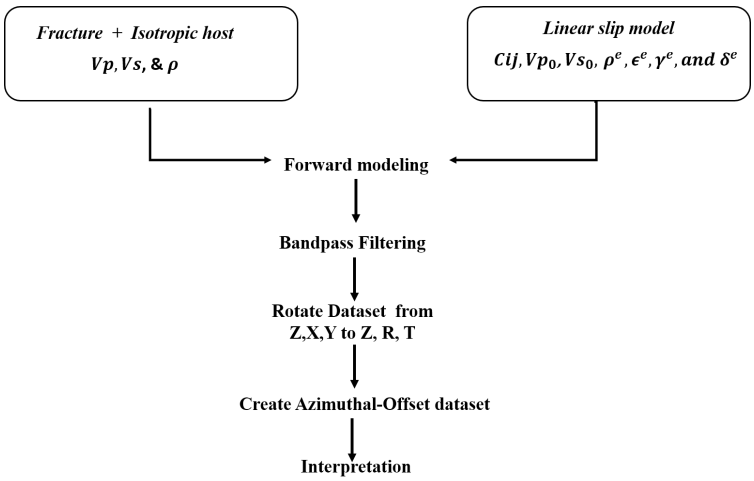

Fig 3b. Workflow

Results

Figure 4 shows the synthetic 3C shot gathers showing P and S-wave reflections propagating along azimuths 0, 15, 60, 90, 105, and 150 degrees to the fracture strike with the fracture strike and normal at 0 and 90 degrees respectively for both models. Vertical (Z), radial (R), and transverse (T) components are shown. Results are overlain with ray-trace traveltime, where red lines indicate P-wave arrivals and blue lines indicate shear wave arrivals. Modeling predicts exact arrival times as raytracing from the top and base of the fractured

media for PP, PPpp, PS and PPss reflections for both models. Notice that the transverse component is zero along 0° and 90° indicating the principal planes of fracturing. Also notice that the transverse datasets measured along non-principal planes are not zero, revealing shear-wave birefringence. Also, the strong multiples and multiple conversions appearing at later times in the Z, R and T datasets of the equivalent modeling, these events are diminished in the dataset from elastic modeling. It is interesting to add that modeling with an isotropic heterogeneous elastic model unlike the homogenous equivalent modeling, will produce a better result without the amplification of multiple and multimodes, thereby enhancing anisotropic processing and imaging especially in scenarios relating to deeply seated fractured reservoirs overlaid by fractured or anisotropic overburden. We can infer that in some circumstances modeling using heterogeneous elastic models might be of higher processing and imaging value than with equivalent media.

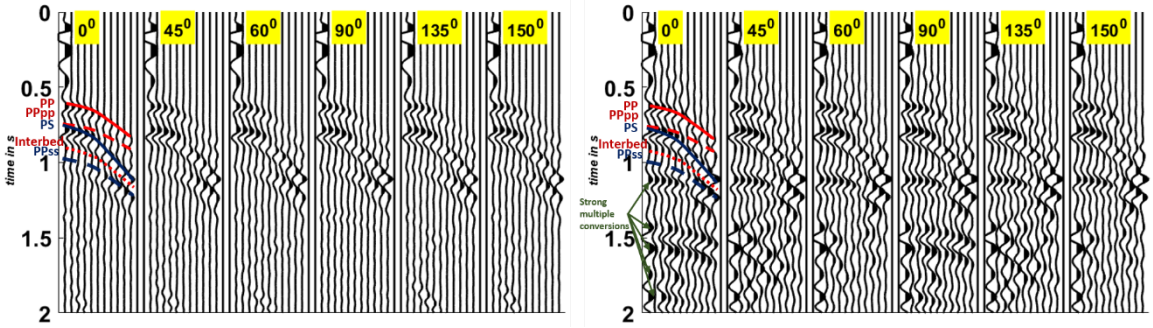

Figure 4a: Vertical, Z, component radial scans showing offset variation at various fixed azimuths. The elastic model is at left and the equivalent model at right. The yellow labels are the azimuthal values in degree.

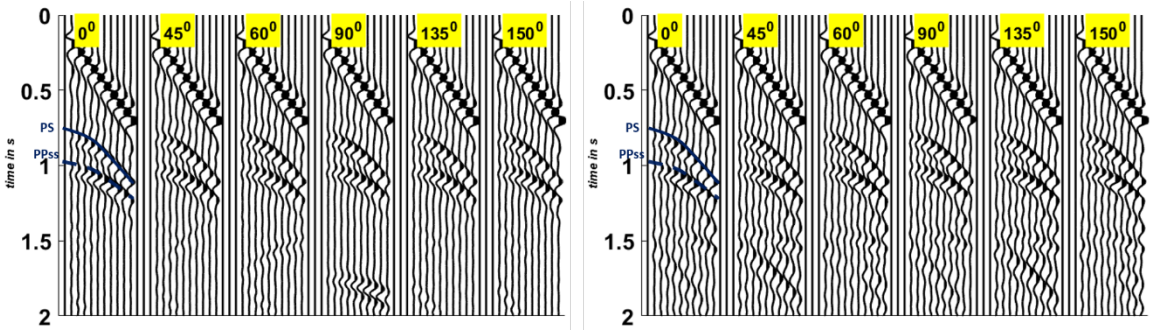

(4b) Similar to 4a but the R (radial) components.

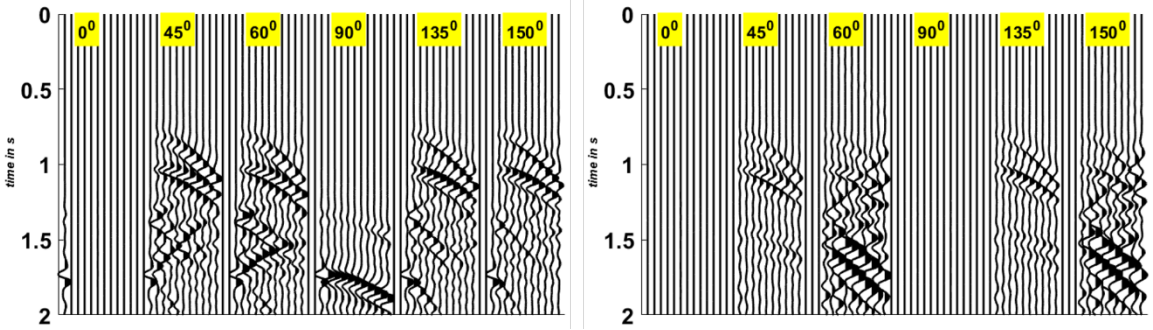

(4c) Similar to 4a but the transverse T components

Data Processing

The recorded 3D-3C datasets (of figure 4 above) was bandpass filtered and rotated into Vertical (Z), Radial (R), and Transverse (T) dataset. We then applied a 2D interpolation on every time slice in order to transform the Z, R, T dataset from its acquisition grid (t, x, y) to the offset-azimuth grid (t, r, φ), where φ denotes azimuths and r denotes source-receiver offset. Figure 5 shows the azimuthal scans of the vertical, radial and transverse datasets at offset of 1.6km for elastic modeling (left) and equivalent modeling (right). The red line and the blue lines indicate the PP and PS primary arrivals from the HTI interfaces and the location of picks. The signature of shear-wave splitting is seen as azimuthal time variation on the $ZRT_{(t,r,\varphi)}$ datasets, but is most clearly diagnosed from the polarity changes observed along the principal axes on the transverse component. We see an overlap between the fast (PS1) and slow (PS2) shear waves in the $Z_{(t,r,\varphi)}$ and $R_{(t,r,\varphi)}$ azimuthal scans. The shear-wave birefringence appears as a sinusoidal event at time 1 seconds and time 1.2 seconds. The transverse component has a distinctly different character. At any intermediate azimuths, the transverse dataset shows shear-wave splitting and the fast and slow shear waves are opposite in polarity. There is no shear wave splitting along isotropy (green arrow) and symmetry axis (orange arrow) where amplitudes drop to zero. These directions are the principal directions or the natural coordinates of fracturing. This characteristic polarity reversal was exploited in several different analyses in this study to determine fracture orientation from shear wave splitting and a key element for recognizing an HTI system. Also, notice the strong multimode event appearing at 1.3 seconds in the elastic modeling (left) which appear much stronger in amplitude in the equivalent medium (right). This is caused by the attenuation due to lateral heterogeneity and irregular scattering within the heterogeneous elastic fractured model. In addition, the transverse component of the equivalent model seems noisier than the elastic model showing the effect of amplified multiples arising from using a homogeneous equivalent model.

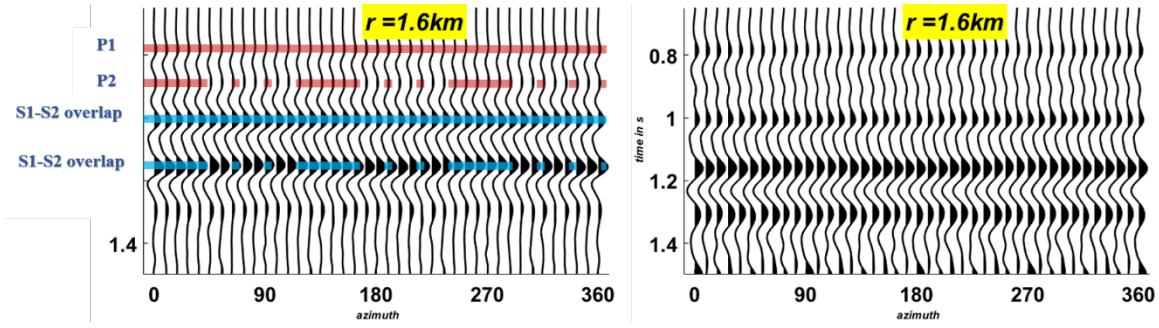

(5a) Z-azimuthal scans. The red and blue line indicates PP and PS primary arrivals from HTI interfaces. The sinusoidal appearance of P waves shows fracture-induced PP azimuthal anisotropy whose imprint grows at increasing offset to depth ratio. Notice the strong multimode event appearing at 1.3 seconds in both models.

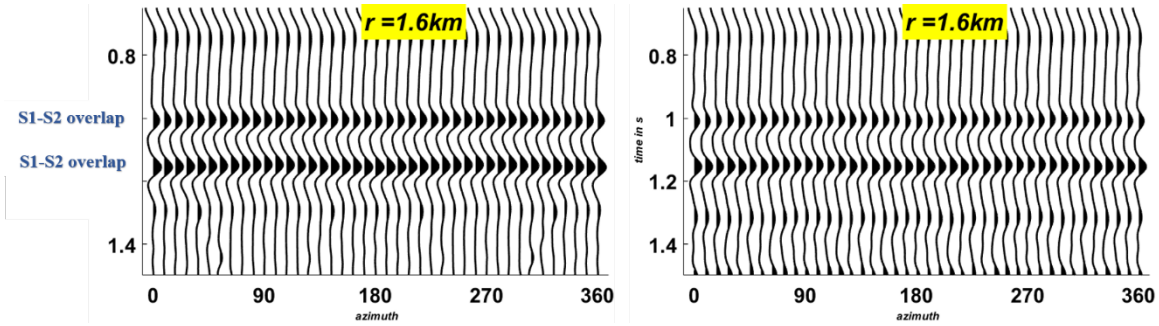

(5b) R-azimuthal scan of elastic modeling (left) and equivalent modeling (right), showing overlap of PS1 and PS2 mode. The sinusoidal appearance at time 1 seconds is the side effect of the overlap between S1 and S2 modes with a time delay between them. Same as at time 1.2 seconds.

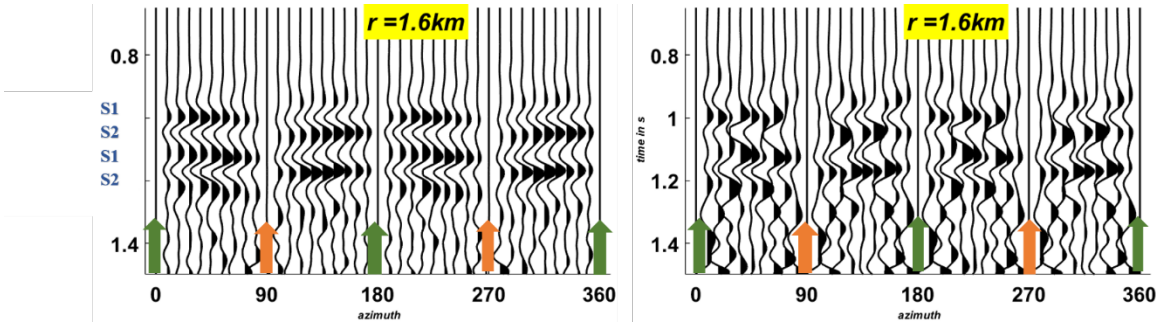

(5c) T-azimuthal scan, showing clear separation of S1 and S2 modes indicating shear wave birefringence. The polarity of both the fast and slow shear waves reverses across the symmetry planes. The green and orange arrows represent the isotropy and symmetry respectively.

Amplitude variation with offset and azimuth (AVOAZ) analysis

Comparing true relative amplitudes with offset, we observe that P-wave reflection amplitude from the elastic and the equivalent modeling both decreases with offset (Figure 6a, b, c, and d) for P wave reflections from the top and base of HTI. Also, the converted wave PS reflection amplitude increases with offset in similar fashion ((Figure 7a, b, c and d) for converted wave reflections from the top and base of HTI. A closer look at amplitude behavior at radial distances of 400, 1000 and 1600m from the center of the source (figure 6e and 6f) reveals that both the elastic modeling and the equivalent modeling predicts close values of reflection amplitudes towards the principal planes and at source receiver offsets comparable to the depth of reflector. We observed that the elastic modeling gave a smoothly varying reflection amplitude result compared with the equivalent modeling. Both the elastic modeling and the equivalent modeling show similar amplitude variation with offset (AVO) behavior comparable to the analytical Ruger AVO behavior (figure 6f). The ruggedness in the equivalent modeling P-wave amplitude plots (figure 6 a-d) are most possibly because the source-generated shear-wave direct arrival artifact generated by the finite difference code is weaker in the elastic than in the equivalent modeling and thus affects the early PP arrivals in the equivalent modeling.

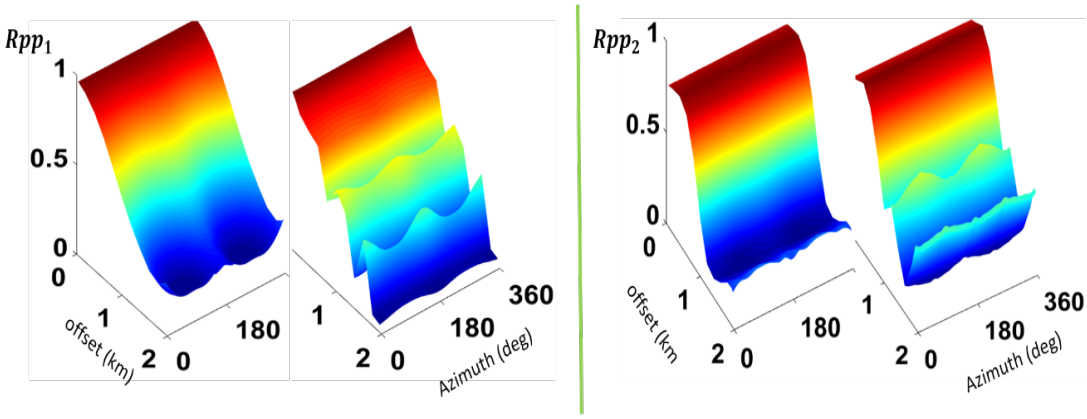

6(a). PP_1 (Elastic modeling) from HTI top

(b). PP_1 (Equiv. modeling) from HTI top

(c). PP_2 (Elastic modeling) from HTI top

(d). PP_2 (Equiv. modeling) from HTI top

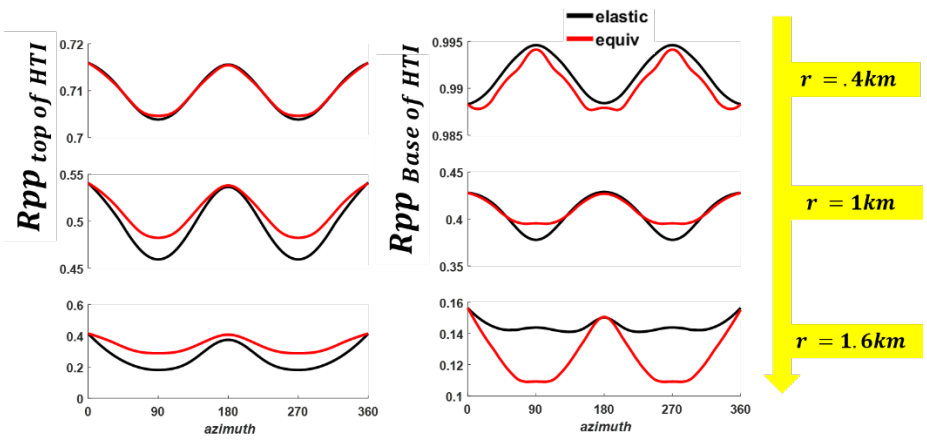

6(e). Amplitude comparison.

Figure 6. (a). Elastic PP reflection AVO/ AVAZ amplitude plot from top of HTI (b). Equivalent PP reflection AVO/ AVAZ amplitude plot from top of HTI (c). Elastic PP reflection AVO/ AVAZ amplitude plot from bottom of HTI (d). equivalent reflection PP AVO/ AVAZ amplitude plot from bottom of HTI (e). Elastic (black) and Equivalent (red) P-wave azimuthal amplitude comparison at .4,1 and 1.6km from HTI top (left) and from HTI bottom (right).

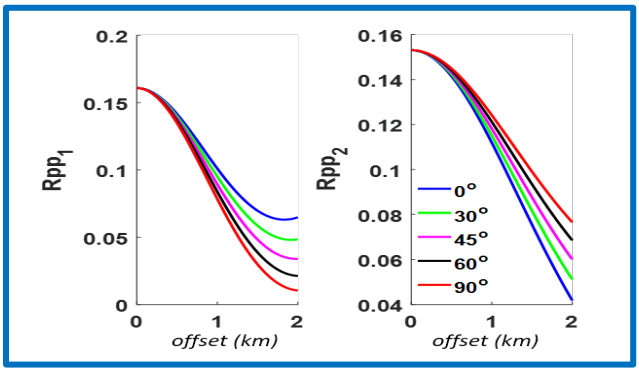

Figure 6f. Analytic results obtained from Ruger approximation for PP1 and PP2 reflections amplitudes from top and bottom of HTI.

Similarly, PS AVO/ AVAZ plot in figure 7(a-e) reveals an overall amplitude increasing with offset, in both elastic and equivalent media for converted wave reflections from the top and bottom of the HTI layer. Again, we see that the equivalent modeling is noisier than the elastic modeling, However, unlike the PP case above, the noise in the PS equivalent modeling is largely as a result of the interference of PS events with multiples and multimode events. We see from comparison of PS amplitude modeling result from the bottom of the HTI layer of figure 7e (right), at near offsets of 0.4 and 1km, that the comparison is noisier for deeper PS events from the bottom of the HTI layer than PS reflections from the top of HTI layer (figure 7e(left)) due to the predominance of multiples at latter arrivals.

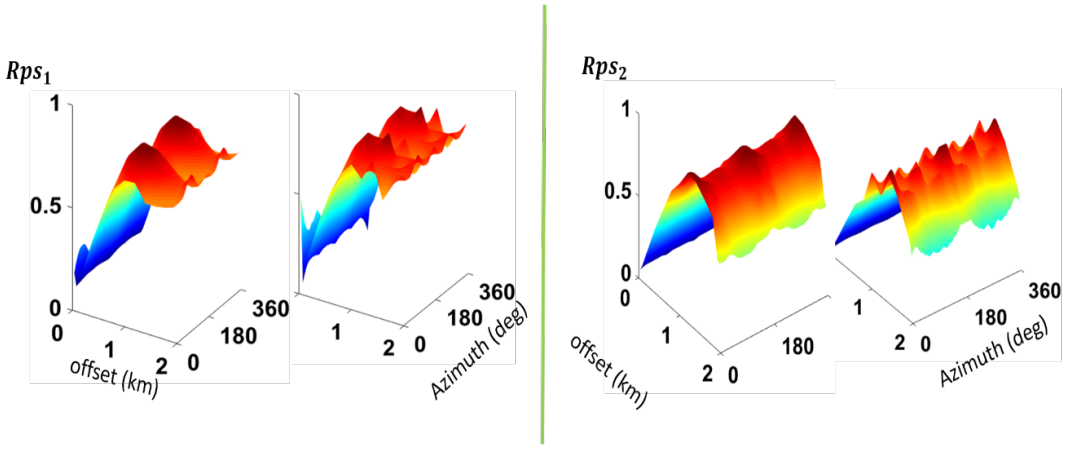

7(a). PS_1 (Elastic modeling) from HTI top

(b). PS_1 (Equiv. modeling)) from HTI top

(c). PS_2 (Elastic modeling) from HTI top

(d). PS_2 (Equiv. modeling)) from HTI top

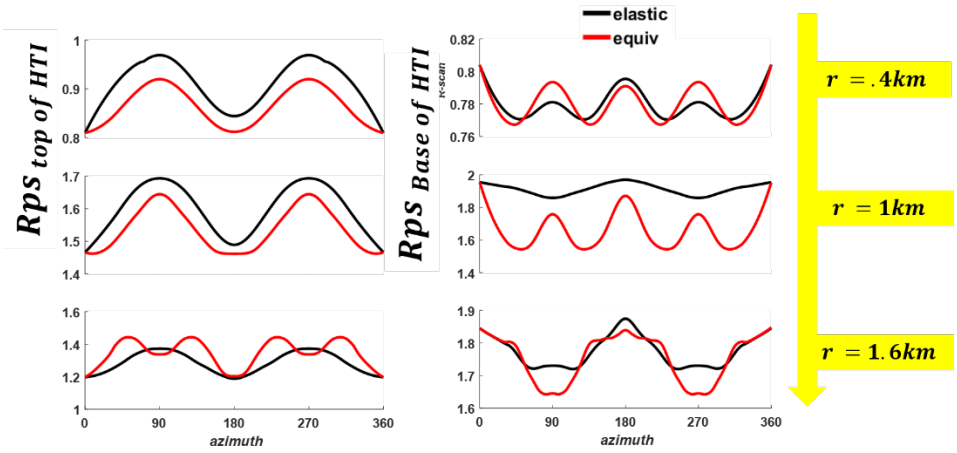

7(e). Amplitude comparison.

Figure 7. (a). Radial component elastic PS AVO/ AVAZ amplitude plot from top of HTI (b). Equivalent PS AVO/ AVAZ amplitude plot from top of HTI (c). Elastic PS AVO/ AVAZ amplitude plot from bottom of HTI (d). Equivalent PS AVO/ AVAZ amplitude plot from bottom of HTI (e). Elastic (black) and Equivalent (red) P-wave azimuthal amplitude comparison at .4,1 and 1.6km from HTI top and (e). Elastic (black) and Equivalent (red) PS-wave azimuthal amplitude comparison at .4,1 and 1.6km from HTI top (left) and from HTI bottom (right).

Figure 8 shows the 2D scans of the vertical, radial and transverse components recorded from the top of the HTI reflector. Note that the onset of azimuthal behavior in both models are much earlier in offset in the radial and transverse component (figure 8b and 8c) compared to the vertical scan PP panel (figure 8a). Also, we see the result of noisy interference from multimode conversions in the equivalent modeling in figure 8a(right), 8b(right) and 8c(right). The elastic modeling (figure 8a(left), 8b(left) and 8c(left)) show clearer offset-azimuth behavior than equivalent modeling. Thus fracture-induced seismic anisotropy is stronger in heterogeneous elastic fractured models than in anisotropic homogenous equivalent models.

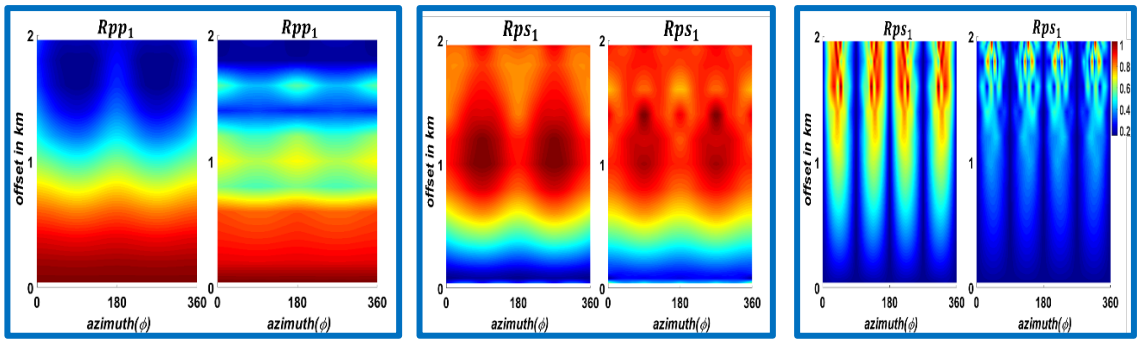

(a)PP, elastic (left), equivalent. (right)

(b). PS-Radial, elastic (left), equivalent. (right)

(c). PS-Transverse, elastic (left), equivalent. (right)

Figure 8. 2D amplitude-offset panels of (a)PP (b). PS-radial component and (c) PS-transverse component obtained from elastic modeling and equivalent modeling.

PP azimuthal amplitude and interval traveltime anisotropy

Given three different offsets (0.4, 1, and 1.6km), we picked the azimuthal amplitudes of P and S waves from first interface of the fractured medium and also computed interval traveltimes within the fractured medium. The PP-wave modeling from polarplots results reveal that P-wave amplitudes show azimuthal variation with respect to offsets in both models. The major axis of the PP-wave amplitude elliptical fit (figure 9a) is in the direction of the fracture strike, this is true for both PP- elastic and equivalent amplitude modeling. We also observed that the major axis of the PP- elastic interval traveltime azimuthal polar plots (figure 9b) is normal to the direction of fracture strike. The PP interval-traveltime plot from equivalent modeling gave no precise direction. However, when studying the effects of fracture on PP anisotropy, we can find that only amplitudes of mid to far offset traces are most suitable for PP anisotropy analysis. In our studies, we find out that amplitude fitting at a near offset of 400m (blue circle) gave an almost circular fit indicating weak PP AVAZ response while farther offsets of 1000m (red ellipse) and 1600m (yellow ellipse) gave strong PP AVAZ response. Equivalent modeling P-wave amplitude azimuthal variation at an offset of 1.6km shows small major to minor axis ratio compared to the elastic

modeling. This may indicate that P-wave fracture-induced anisotropy may vary slightly for both models especially at long offset and are weaker in equivalent models as seen in figure 9a. Also the azimuthal interval traveltime analysis of figure 9b shows that fracture-induced P-wave traveltime anisotropy in both elastic and equivalent models are not very evident at small offset.

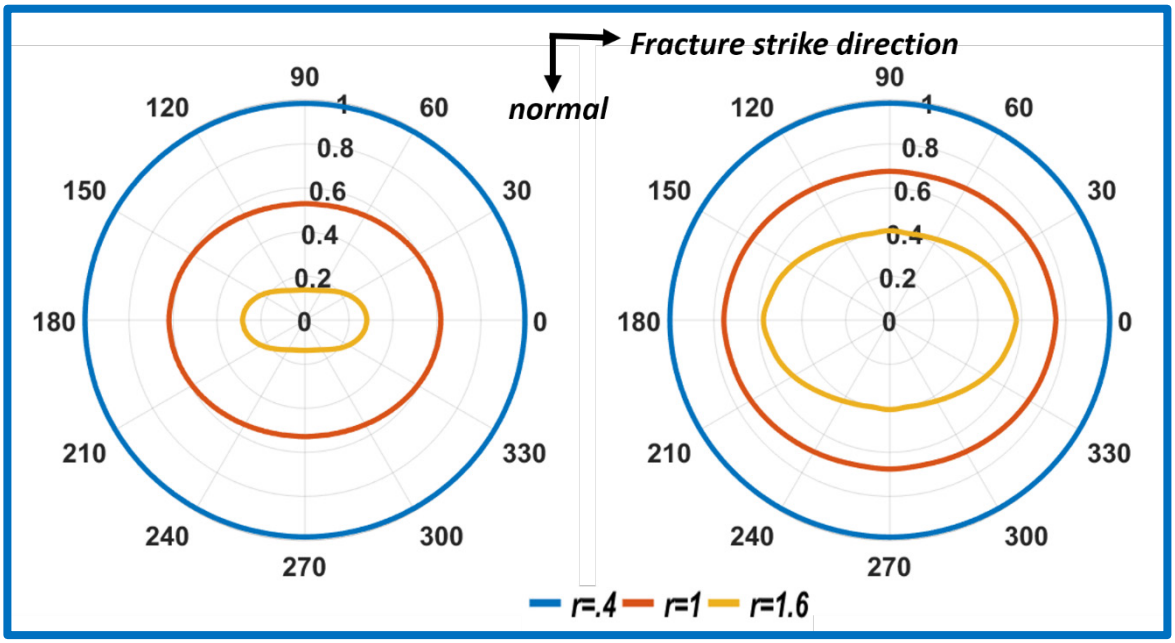

(9a). Azimuthal polar plot of PP scaled reflection amplitude azimuthal anisotropy from top of HTI layer for elastic (left) and equivalent modeling (right), major axis is in the fracture strike direction

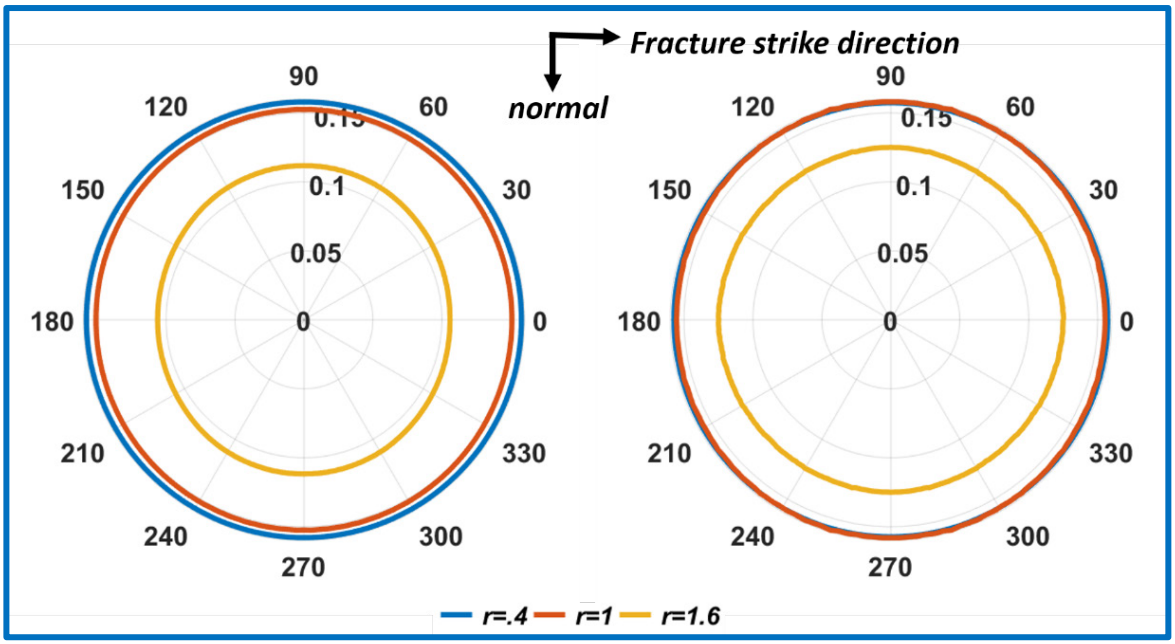

(9b). Azimuthal polar plot of PP scaled interval traveltime within the top and bottom of the fractured layer, for elastic (left) and equivalent modeling (right), major axis is normal to the strike direction. The equivalent modeling is noisier along symmetry.

PS azimuthal amplitude and interval traveltime anisotropy

Figure 10a shows that, at offsets of 0.4, 1, and 1.6, the converted wave PS reflection amplitudes of the R-component from the top of the fractured medium have a stronger elliptical distribution than the PP-waves. We also see that the near offset PS reflections (e.g. 400m offset below) is stronger than the P-wave amplitudes polar plot in figure 9a above for the same near offset. We can see that shear-wave amplitude anisotropy have an earlier onset of azimuthal amplitude variation than P-wave reflection amplitude anisotropy. The equivalent modeling amplitude polar plot appear noisier especially at large offset shown by the yellow line). In contrast to the PP-wave refection amplitude plot in figure 9a, where the major axis of the ellipse indicates the direction of the fracture strike, the major axis in the R- component PS-amplitude analysis, is normal to the fracture strike. Further comparison of figure 9a and 10b, we noticed that the PS-waves amplitudes show earlier onset of observable amplitude anisotropy than P-waves (see blue line in both figures), and a wider applicable offset range than PP-waves for several amplitude analysis. Figure 10b shows that, the T-component amplitude polarplot from the top of the fractured layer show an obvious azimuthal dependence with zero-crossings and amplitude polarity reversals, which is very similar to the pattern observed in figure 8c.

Figure 10c shows the azimuthal interval traveltimes from elastic and equivalent modeling. The modeling results shows that the azimuthal variation of interval traveltimes of the R-component waves show weak elliptical distribution in both elastic and equivalent models. Notice, that the major axes of the PP and PS amplitude azimuthal plots gave indication of fracture orientations than the PP and PS interval traveltime azimuthal plots. This is also true if offset is not long enough and worse so in equivalent modeling.

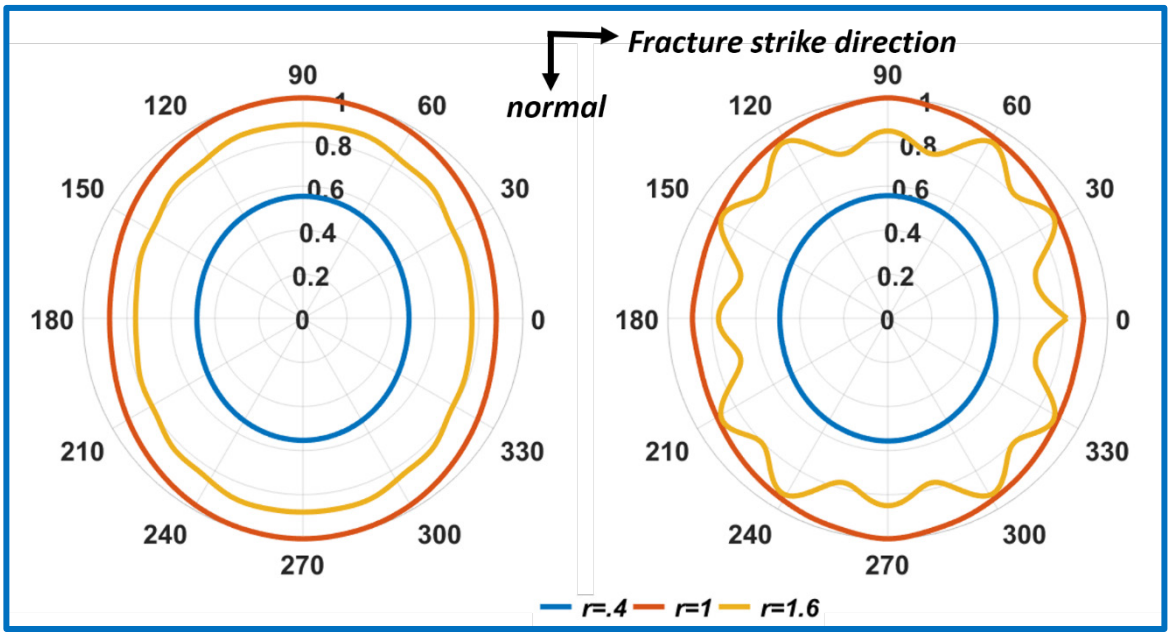

(10a). Azimuthal polar plot of PS anisotropy- Radial component for elastic (left) and equivalent modeling (right), major axis is normal to strike direction.

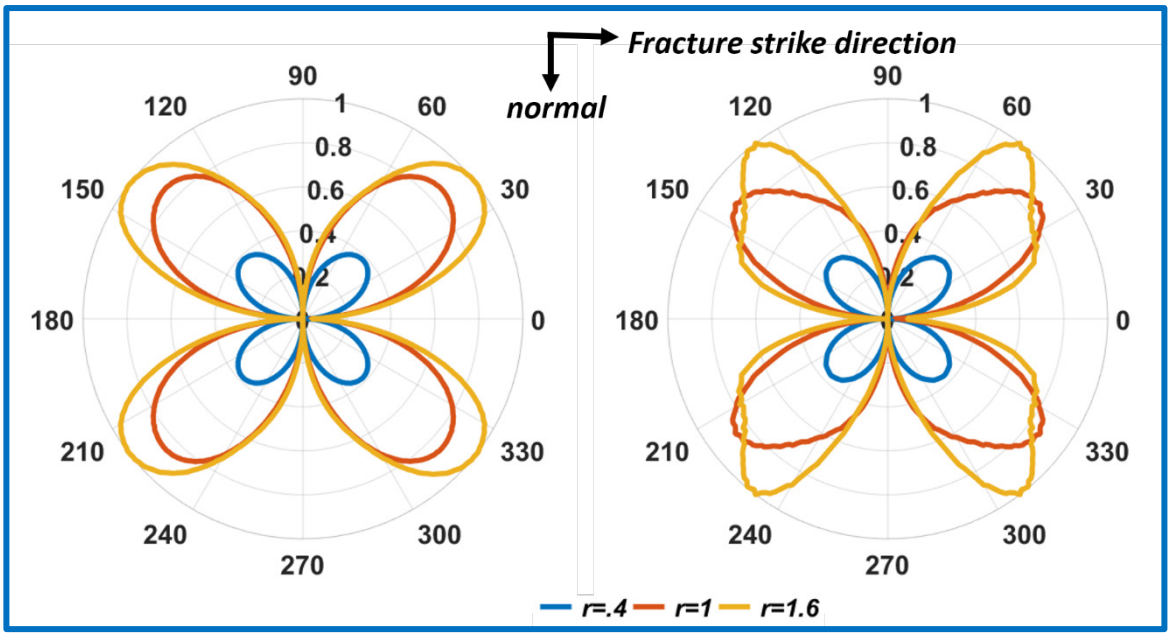

(10b). Azimuthal polar plot of PS anisotropy- Transverse component for elastic (left) and equivalent modeling (right), zero crossings points to natural coordinates of fracture.

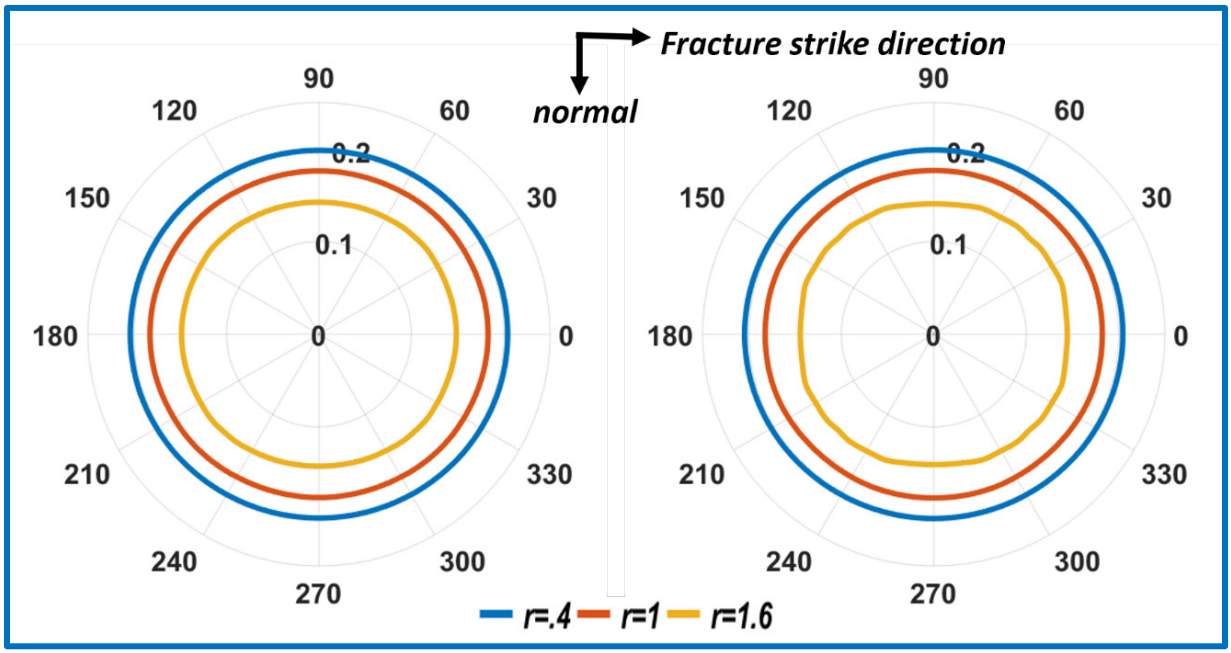

(10c) Azimuthal polar plot of PS interval traveltime within the top and bottom of the fractured layer for elastic (left) and equivalent modeling (right), major axis is in the direction of strike

CONCLUSIONS

We have successfully carried out a 3D numerical modeling and comparison of a vertically fractured isotropic heterogeneous elastic model and anisotropic homogeneous equivalent model with the goal of understanding the benefits of using either of these model types in understanding anisotropic responses and noise in multicomponent data. We explored the differences in PP AVOAZ and PS AVOAZ responses from these two models. We observed that the homogeneous equivalent modeling is susceptible to strong multiple and multimode interferences than the isotropic heterogeneous elastic model. This is because the heterogeneous medium causes irregular scattering of the multiple and multimode events. We can infer that in some circumstances modeling using heterogeneous elastic models might be of higher processing and imaging value than with equivalent media. We have seen that the amplitudes of PP-waves and the radial component of PS-waves are distributed in a relatively elliptical manner, while the amplitudes of the transverse component show zero-crossings and polarity reversals. We have also observed that PS-waves amplitudes show a wider applicable offset range and a larger observable azimuthal anisotropy than PP-waves. This statement is true for both elastic and equivalent modeling. We also observe that fracture orientation detection from PP and PS reflection amplitudes azimuthal analysis gave better result than the azimuthal analysis of PP- and PS interval traveltime in both models. The major axis of the PS-wave elliptical fit from radial dataset points to the fracture normal direction and opposite to the major axis of the PP amplitude azimuthal analysis whose major axis is in the fracture strike direction. In general, both modeling accurately predicts the traveltime arrivals of the primary PP and PS reflections and multimode for the two HTI models, however the multimode amplitudes predicted by homogenous equivalent modeling is stronger than the multimodes in the heterogeneous elastic models. These

multimodes have the tendency to mask primary PP and PS events, thus the elastic modeling result is less noisy and will be less tedious for further processing and interpretation. The next immediate work will be to carry out an AVAZ inversion of the numerical datasets and compare the results from both models. We will also like to extend our analysis to a case of an orthorhombic model overlaid with finely layered overburden which is more relatable to field records.

ACKNOWLEDGEMENTS

This work was funded by CREWES industrial sponsors and NSERC (Natural Science and Engineering Research Council of Canada) through the grant CRDPJ 461179-13. The authors thank the sponsors of CREWES for continued support. The first author also gratefully acknowledges Faranak Mahmoudian, Kevin Hall, and Raul Cova for their assistance.

REFERENCES

Al Dulaijan and Margrave, G. F. 2016, VVAZ analysis for seismic anisotropy in the Altamont-Bluebell Field, 86th Annual International Meeting, SEG, Expanded Abstracts.

Backus, G. E., 1962, Long-wave elastic anisotropy produced by horizontal layering: Journal of Geophysical Research, 67, 4427–4440.

Bakulin, A., Grechka, V., and Tsvankin, I., 2000, Estimation of fracture parameters from reflection seismic data. Part I: HTI model due to a single fracture set: Geophysics, 65, 1788–1802.

Bale, R., B. Gratakos, B. Mattocks, S. Roche, K. Poplavskii, and X. Li, 2009, Shear wave splitting applications for fracture analysis and improved imaging: Some onshore examples: First Break, 27, 73–83.

Carcione, J.M., Picotti, S., Cavallini, F., Santos, J.E., 2012. Numerical test of the Schoenberg-Muir theory. Geophysics 77, 27-35.

Daley, P.F. and Hron, F., 1977, Reflection and transmission coefficients for transversely isotropic media, Bulletin of the Seismological Society of America, **67**, 661-675.

Hudson, J. A., 1981, Wave speeds and attenuation of elastic waves in material containing cracks. Geophysical Journal Royal Astronaut Society, 64, 133 – 150.

Liu, E., Hudson, J. A., and Pointer, T., 2000. Equivalent medium representation of fractured rock: Journal of Geophysical Research, 105, 2981 – 3000.

Mahmoudian, F., Margrave, G.F., Wong, J., and Henley, D.C, 2013, Fracture orientation and intensity from AVAz inversion: A physical modeling study. 83th Annual International Meeting, SEG, Expanded Abstracts.

Qian, Z., Li, X-Y., Chapman, M., 2007, Azimuthal variations of PP- and PS-wave attributes: a synthetic study: 77th Annual International Meeting, SEG, Expanded Abstracts, 184–187.

Rüger A. 1996, Variation of P-wave reflectivity with offset and azimuth in anisotropic media: 66th Annual International Meeting, SEG, Expanded Abstracts, 15, 1810–1813.

Schoenberg, M. and Douma, J., 1988, Elastic-wave propagation in media with parallel fractures and aligned cracks: Geophysical Prospecting, EAGE., 36,571-590.

Schoenberg, M., and Muir, F., 1989, A calculus for finely layered media: Geophysics, 54, 581–589,